POTENTIAL VORTICITY EVOLUTION OF A PROTOPLANETARY DISK WITH AN EMBEDDED PROTOPLANET

Hui Li,[1] Shengtai Li,[2] Josef Koller,[3] Burton B. Wendroff,[2] Richard Liska,[2,4]
Chris M. Orban,[5] Edison P. T. Liang,[6] and Douglas N. C. Lin[7]

ABSTRACT

We present two-dimensional inviscid hydrodynamic simulations of a protoplanetary disk with an embedded planet, emphasizing the evolution of potential vorticity (the ratio of vorticity to density) and its dependence on numerical resolutions. By analyzing the structure of spiral shocks made by the planet, we show that progressive changes of the potential vorticity caused by spiral shocks ultimately lead to the excitation of a secondary instability. We also demonstrate that very high numerical resolution is required to both follow the potential vorticity changes and identify the location where the secondary instability is first excited. Low-resolution results are shown to give the wrong location. We establish the robustness of a secondary instability and its impact on the planet's torque. After the saturation of the instability, the disk shows large-scale nonaxisymmetry, causing the torque on the planet to oscillate with large amplitude. The impact of the oscillating torque on the protoplanet's migration remains to be investigated.

Subject headings: accretion, accretion disks — hydrodynamics — planetary systems: protoplanetary disks

1. INTRODUCTION

Well before extrasolar planets were discovered, Goldreich & Tremaine (1979, 1980) and Lin & Papaloizou (1986a, 1986b) speculated that tidal interactions between disks and embedded protoplanets would lead to planet migration. Ward (1997) suggested that two different types of migration could occur. One, called type I migration, takes place when the protoplanet mass is still small enough that the migration rate can be evaluated using linear analysis; it is shown to be quite fast in the sense that the migration timescale is shorter than the estimated buildup timescale of a giant protoplanet core. This has presented a serious problem for the formation of giant planets. The other, called type II migration, takes place when the protoplanet is massive enough that it opens gaps in the disk. The protoplanet is then locked into the disk's viscous evolution timescale, which is typically long.

The discovery of extrasolar planets with a large number of short-period planets very close to their parent stars seems to support a migration scenario, since it is more likely that giant planet formation takes place at larger distances outside the snow line. This has generated renewed interests in the study of tidally induced planet migration (e.g., Kley 1999; Lubow et al. 1999; Nelson et al. 2000; D'Angelo et al. 2003). Both types of migration have been basically confirmed by nonlinear numerical simulations, although most simulations to date are performed with a prescribed viscosity.

A recent study by Balmforth & Korycansky (2001) focused on the evolution of potential vorticity (PV) in the co-orbital region of a planet, and they noted the possibility of secondary instabilities in the corotation resonance region, which lead to the formation of vortices. They showed that nonlinear dynamics of the co-orbital region have an important influence on the saturation of the corotation torque.

In an earlier paper (Koller et al. 2003), we also investigated the nonlinear dynamics in the co-orbital region (within ~10 Roche lobe radii of the planet) through global, nonlinear two-dimensional inviscid simulations. We found that the PV of the disk flow undergoes systematic changes, presumably caused by the spiral shocks generated by the planet, although we did not give any detailed analysis of the shocks. We also found that the flow eventually becomes unstable because of the inflexion points in the PV profile. Vortices are formed as a consequence.

This paper is a close follow-up to Koller et al. (2003). Our purpose is twofold. First, we present quantitative analyses of the ways that shocks change the PV of the flow. Second, through extensive numerical resolution studies, we confirm the physical mechanism for exciting a secondary instability through inflexion points in the PV profile. However, we now find that the instability is excited at a different location from what Koller et al. presented. The phenomenon observed by Koller et al. is apparently due to limited numerical resolutions and is thus artificial. Nevertheless, we are still able to demonstrate the existence of such a secondary instability and its impact on the planet's torque. We have also performed extensive numerical tests via different resolutions to check the validity of these new findings.

This paper is organized as follows. We first describe our numerical approach and our setup of simulations in § 2 and § 3. We then present the analyses of shocks and the ways they change the PV in § 4. The excitation of a secondary instability is described in § 5. The influence of numerical resolution is presented in § 6. Discussions are given in § 7.

2. NUMERICAL MODEL

We assume that the protoplanetary disk is thin and can be described by the inviscid two-dimensional isothermal Euler equations in a cylindrical (r, ϕ) plane with vertically integrated

[1] Applied Physics Division, MS B227, Los Alamos National Laboratory, NM 87545; hli@lanl.gov.

[2] Theoretical Division, MS B284, Los Alamos National Laboratory, NM 87545; sli@lanl.gov, bbw@lanl.gov.

[3] ISR Division, MS D466, Los Alamos National Laboratory, NM 87545; jkoller@lanl.gov.

[4] Faculty of Nuclear Sciences and Physical Engineering, Czech Technical University, Prague, Czech Republic; liska@siduri.fjfi.cvut.cz.

[5] Department of Astronomy, University of Illinois at Urbana-Champaign, Urbana, IL 61801; corban@uiuc.edu.

[6] Department of Physics and Astronomy, Rice University, Houston, TX 77005; liang@spacsun.rice.edu.

[7] UCO/Lick Observatory, University of California, Santa Cruz, CA 95064; lin@ucolick.org.

quantities. The differential equations are the same as those given in Kley (1998). Simulations are carried out mostly using a split dimension hydrocode (S. Li & H. Li 2005, in preparation), whose basic algorithm is based on the MUSCL-Hancock scheme (MHS; Toro 1999). The methodology of MHS is extended here for the presence of source terms with the following two main modifications: the fluxes are computed using primitive instead of conserved variables, where the van Leer flux limiter is applied to the slopes of the primitive variables, and an iterative approximate Riemann solver is used. Standard dimensional splitting and some source splitting are used. Radial sweeps with the angular flux derivatives omitted are alternated with angular sweeps with the radial flux derivatives omitted. All source terms except the planet's gravitational force are included in the radial sweep. The planet force is applied in a separate sweep as the numerical gradient of the planet potential, so the numerical curl of this gradient is zero, minimizing the PV contamination by the planet.

We use the local comoving angular sweep as proposed in the FARGO scheme of Masset (2000) and modified in Li et al. (2001). The idea is basically to use a semi-Lagrangian form for the transport terms in the angular sweep. A constant velocity is subtracted from the angular transport velocity. This velocity is chosen to be close to the mean angular velocity, in order to move the data an integral number of angular cells in one time step. This is then corrected by an integral shift of the data. This enables us to use a much larger time step than would otherwise be possible.

The MHS scheme requires two ghost cells in the radial sweep (the angular sweep is periodic). Holding these ghost cells at the initial steady state produced the smallest boundary reflection of all boundary conditions tried.

3. INITIAL SETUP

The two-dimensional disk is modeled in the range $0.4 \leq r \leq 2$. The planet is assumed to be on a fixed circular orbit at $r = 1$. A corotating frame is used, and the positions of the central star and the planet are fixed at $(r, \phi) = (0, 0)$ and $(r_p, \phi_p) = (1, \pi)$ (acceleration due to frame rotation is also included; see Kley 1998). The mass ratio between the planet and the central star is $\mu = M_p/M_*$. Its Hill (Roche) radius is $r_H = r_p(\mu/3)^{1/3}$. The disk is assumed to be isothermal with a constant temperature throughout the simulation region. The isothermal sound speed, scaled by the Keplerian rotation speed v_ϕ at $r = 1$, is $c_s/v_\phi = H/r$, where H is the disk scale height. Time is measured by the orbital period at $r = 1$.

We choose an initial surface density profile with $\Sigma(r) \propto r^{-3/2}$ so that the ratio of vorticity to surface density, potential vorticity (PV $\equiv \zeta$), has a flat radial profile $\zeta = (\nabla \times \boldsymbol{v})_z/\Sigma \approx \text{const.} \approx 0.5$. (Note that ζ has a small deviation from being precisely 0.5 because of the finite pressure gradient that slightly modifies v_ϕ from its Keplerian value.) With this initial condition, we avoid the generation of inflection points due to the rearrangement of ζ distribution as it is carried by the stream lines (Balmforth & Korycansky 2001).

We typically run the disk without the planet for 10 orbits first so that the disk is settled into a numerical equilibrium (very close to the analytic one). Then the planet's gravitational potential is gradually "turned on" over a 10 orbit period, allowing the disk to respond to the planet potential gradually. Furthermore, the planet's potential is softened by an approximate three-dimensional treatment. The basic idea is that, at any location (r, ϕ), the matter with surface density Σ is distributed (divided into many cells) vertically over many scale heights (say, $\pm 6H$) according to a Gaussian isothermal profile. Radial and azimuthal forces exerted by the planet at a specific (r, ϕ, z) are calculated in this three-dimensional fashion. To get the two-dimensional radial and azi-

muthal forces for a specific (r, ϕ), one then integrates all the cells along z. Comparing this pseudo–three-dimensional treatment with the usual two-dimensional treatment in which a fixed smoothing distance is used, this pseudo–three-dimensional treatment reduces the force close to the planet (within $\sim 2r_H$) by about a factor of 2 but converges to the usual two-dimensional force beyond $\sim 5r_H$. Although there is some accumulation of gas near the planet, we do not allow any disk gas to be accreted onto it. Self-gravity of the disk is not included. Runs are made using several radial and azimuthal grids to study the influence of resolution, which ranges from $(n_r \times n_\phi) = 200 \times 800$ to 1200×4800. Simulations typically last several hundred orbits at $r = 1$.

One key feature of our simulations is that they are performed at the inviscid limit; i.e., we do not explicitly include a viscosity term, although numerical viscosity is inevitable and is needed to handle shocks. In addition, our simulations tend to be of higher resolution. With a radial $n_r = 800$ (some runs go up to $n_r = 1200$, $n_\phi = 4800$) and $0.4 \leq r \leq 2$, the diameter of the Hill sphere of a planet with $\mu = 10^{-4}$ is resolved by ~ 32 cells in each direction.

4. SHOCK STRUCTURE AND PV CHANGES

We use one run in this section to facilitate discussion. This run has $\mu = 10^{-4}$, $c_s = 0.05$, $r_H = 0.0322$, and a $n_r \times n_\phi = 800 \times 3200$ resolution. Figure 1 shows the surface density (multiplied by $r^{1.5}$ so that the background surface density is unity initially) in the (r, ϕ) plane at $t = 100$ orbits. It shows the characteristic density enhancement at the planet and at the two spiral shocks. Two density "depressions" at $|\Delta r| \sim 3 - 4r_H$ are developed as angular momentum is gradually deposited there. Two density bumps (enhancements) occur broadly over $|\Delta r| \sim 5 - 8r_H$. Here $\Delta r = r - r_p$. Some streamlines (in the corotating frame) are plotted as well.

4.1. *PV Change by Shocks*

Figure 2 shows the azimuthally averaged $\langle \zeta \rangle$ profile from $t = 40$, 100, 160, 220, and 300 orbits. (The initial value ≈ 0.5 is subtracted.) Several features can be seen. First, there are very small changes in $\langle \zeta \rangle$ for $|\Delta r| \leq 2r_H$. Second, at larger distances from the planet, $\langle \zeta \rangle$ profile changes progressively with time and shows both an increase and decrease from its initial value. An interesting feature is that even though both "peaks" and "valleys" are growing with time, two locations around $\Delta r = \pm 4.5r_H$ have no change in $\langle \zeta \rangle$. A natural question is what causes these features.

The flow around the planet can be separated into several subregions depending on their streamline behavior (e.g., see Masset 2002), including the horseshoe (or librating) region with $|\Delta r| \leq r_H$, the separatrix region $r_H < |\Delta r| < \sqrt{12}r_H$, and the streaming region $|\Delta r| > \sqrt{12}r_H$. Typically, spiral shocks do not occur until the relative velocity between the disk flow and the planet becomes larger than the sound speed. This roughly translates to $|\Delta r| \approx H$. So a critical parameter is $H/r_H \approx c_s/r_H$, which gives an indication of whether the spiral shock is starting from within the planet's Roche lobe (see also Korycansky & Papaloizou 1996). In the limit of small c_s/r_H, flow around the planet becomes quite complicated (e.g., see Tanigawa & Watanabe 2002). An additional yet potentially very important complication is that any numerical error coming out nearing the planet might be strongly amplified by these shocks, giving numerical artifacts that can be physically unreal. Thus, we have mostly used a relatively higher sound speed of $c_s = 0.05$ ($> r_H$) in this study. Higher sound speeds mean weaker shocks, which typically also mean slower changes in the disk properties.
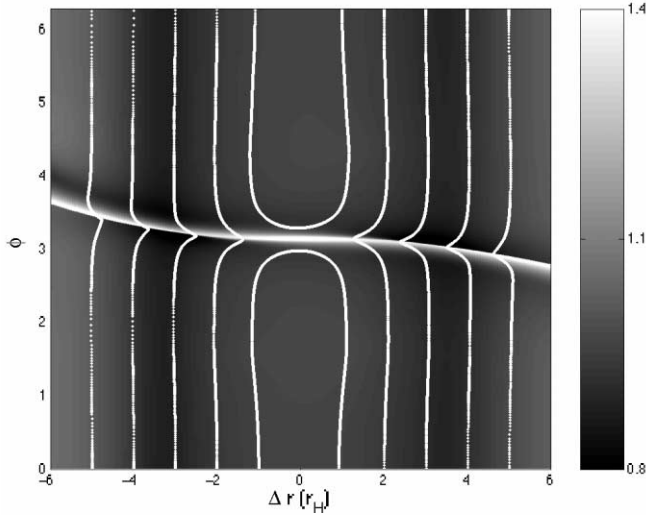
Fig. 1.—Surface density, multiplied by $r^{1.5}$, in the (r, ϕ) plane at $t = 100$ orbits for a run with $\mu = 10^{-4}$, $c_s = 0.05$, and $n_r \times n_\phi = 800 \times 3200$. (The initial background surface density is unity, after multiplying by $r^{1.5}$.) The planet is located at $\Delta r = 0$ and $\phi = \pi$. Two spiral shocks cut through the disk, bending stream lines. The PV changes induced by the shock are transported to different radii from their production site.

As discussed in Koller et al. (2003), spiral shocks are capable of destroying the conservation of PV. For the parameters used in this run, we do not expect shocks within $\sim \pm 2 r_{\mathrm{H}}$, which is confirmed by the fact that $\langle \zeta \rangle$ stays roughly at the initial value. Once in the shocked region, we can use a very useful formula for calculating the PV jump across a (curved) shock, which is given in Kevlahan (1997), after some manipulation,

$$\Delta \zeta = \frac{(M_\perp^2 - 1)^2}{M_\perp^2} \frac{\partial M_\perp}{\partial \tau} \frac{c_s}{\Sigma_2}, \qquad (1)$$

where $M_\perp$ is the perpendicular Mach number $(u_\perp / c_s)$ that is equal to $(\Sigma_2 / \Sigma_1)^{1/2}$ for isothermal shocks. Here Σ_1 and Σ_2 are the pre- and postshock surface densities. The direction τ is tangential to the shock front and is defined to be pointing away from the planet.
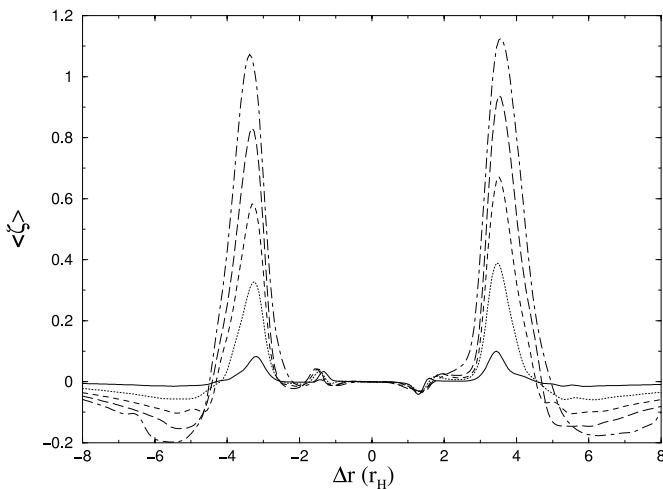

Fig. 2.—Azimuthally averaged $\langle \zeta \rangle$ profile at $t = 40$ (solid curve), 100, 160, 220, and 300 (dot-dashed curve) orbits for a run with the same parameters as in Fig. 1. The planet is located at $\Delta r = 0$. The initial radial profile $\zeta \approx 0.5$ has been subtracted. Note the progressive growth of peaks and valleys in the $\langle \zeta \rangle$ profile. In addition, $\langle \zeta \rangle$ in the planet region remains roughly unchanged.
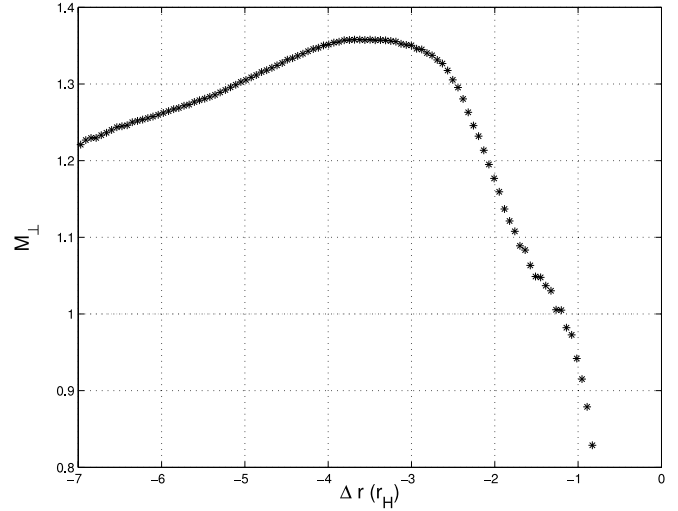

Fig. 3.—Perpendicular Mach number $M_\perp$ along the spiral shock front for the run shown in Fig. 1 at $t = 100$ orbits. Note that the radial distances here mark the PV production sites, to which systematic shifts shown in Fig. 1 have to be added when compared with the radial locations in Fig. 2.

According to equation (1), the sign of $\Delta \zeta$ is determined only by the gradient of $M_\perp$ along the shock front.

Figure 3 shows $M_\perp$ as a function of radial distance to the planet (only one side is shown). This is obtained by first identifying the high compression region through calculating the velocity compression. After finding the flow impact angle to that surface, one can then calculate $M_\perp$ at the shock. Differentiating along that surface gives $\partial M_\perp / \partial \tau$. This figure shows the general behavior of what one might expect of a spiral shock produced by the planet. As one moves away from the planet radially, the flow goes from a nonshocked state to having shocks, which means that $M_\perp$ gradually increases from being <1 to 1 when the shock actually starts. Very far away from the planet, the pitch angle between the spiral wave and the background flow becomes small enough that $M_\perp$ is expected to become <1 again. Thus, as a function of radial distance from the planet, $M_\perp$ is expected to increase first, reaching its peak; then starting to decrease, it eventually drops to be <1 at some large distance. Consequently, using equation (1), we can expect that $\Delta \zeta$ is positive at first, becomes zero when $M_\perp$ is reaching its peak, and then is negative when $M_\perp$ is decreasing. This matches quite well the behavior of $\langle \zeta \rangle$ given in Figure 2. Note that over the whole evolution, shocks are quite steady with very slow evolution, indicated by the small "outward" movement of the inflexion points (where $\Delta \zeta \approx 0$). All these features are quite generic, and we have confirmed this by using several different planet masses.

From Figure 3 we can see that $M_\perp$ peaks at $\Delta r \approx -3.8 r_{\mathrm{H}}$, but the point where $\Delta \zeta = 0$ is at $-4.5 r_{\mathrm{H}}$ based on Figure 2. To quantitatively match the two profiles in terms of radial distances to the planet, one has to take into account the fact that the radial location where shock occurs (and the flow's PV is changed) is different from where these PV changes are eventually deposited. This is illustrated in Figure 1. Correcting for this systematic shift in radial locations, the agreement between the azimuthally averaged $\langle \zeta \rangle$ profile and the $M_\perp$ profile is quite good.

To summarize, the spiral shocks emanating close to the planet cause systematic changes to the PV distribution of the disk flow. As the disk rotates, the disk flow repeatedly passes through these shocks so that changes in PV then accumulate. The sign of PV change is determined by the shock structure, and the amplitude of change is determined by both the shock structure (eq. [1]) and
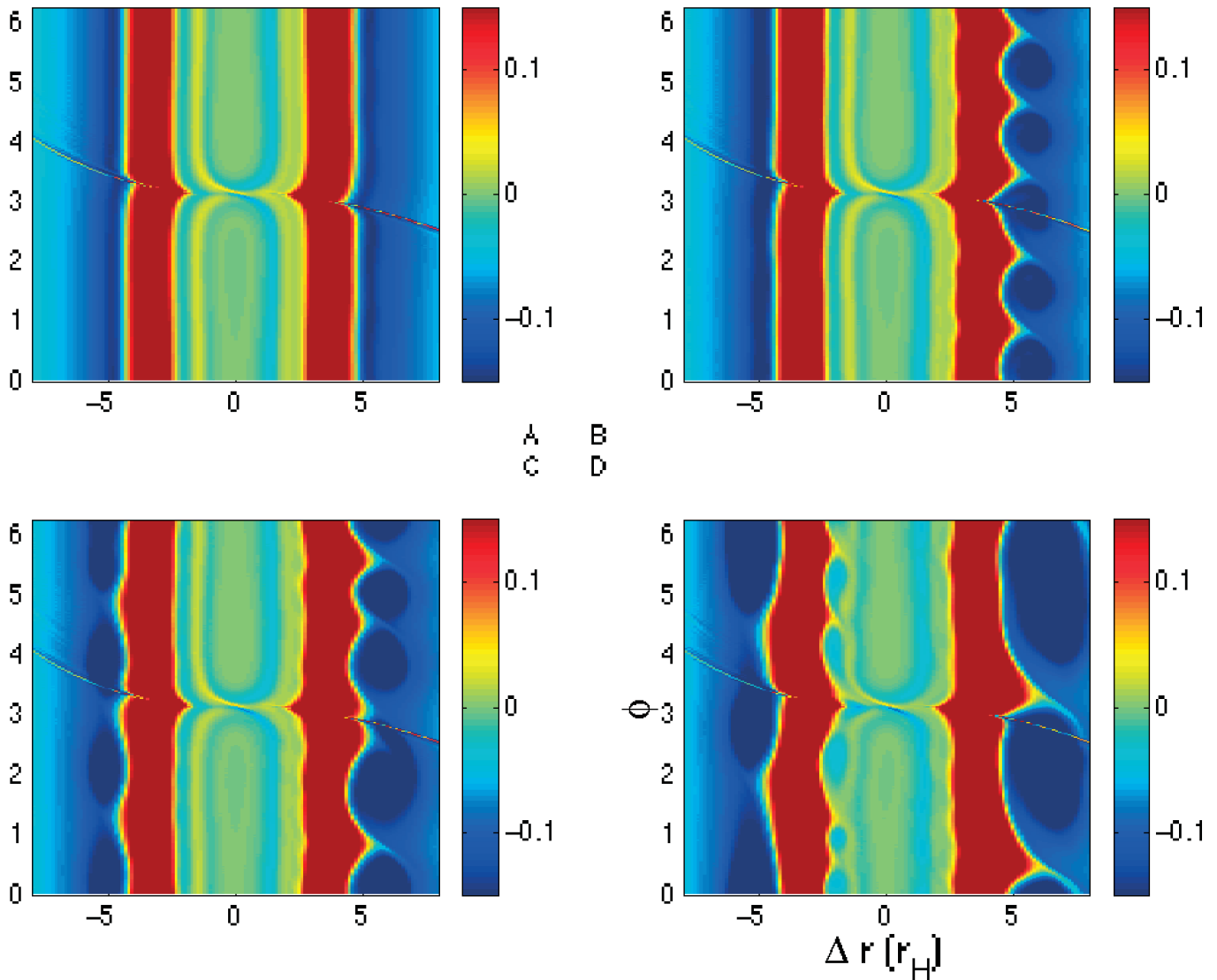
FIG. 4.—PV in the (r, ϕ) plane at $t = 160, 180, 200,$ and 240 orbits (*panels a–d, respectively*) with $n_r \times n_\phi = 400 \times 1600$. (Results are similar for other resolutions.) (*b*) and (*c*) show the initiation of a secondary instability in the valley regions with $|\Delta r| = 5 - 7r_H$. This instability breaks the flow into higher density blobs ("vortices"), which are indicated by the isolated PV depressions (*b, c*). These vortices merge at late times, forming large-scale asymmetries in the azimuthal direction (*d*).

how many times the flow passes through the shocks in a given time $[\sim(r^{-3/2} - 1)\Delta t/2\pi]$. We have identified the physical cause for having both positive and negative changes in PV, in addition to the existence of an inflexion point. We defer the quantitative comparison of the amplitude of PV changes between simulations and equation (1) to a future study.

5. SECONDARY INSTABILITY

5.1. *Instability and Vortices*

Having established the profile of $\langle \zeta(r, t) \rangle$, we now turn to the issue of secondary instability. This type of instability is usually associated with the existence of inflexion points (extrema) in the PV profile (see Drazin & Reid 1981) and often requires satisfying a threshold condition. As shown in Figure 2 the PV profile has extrema points, and the magnitude of the slope between the peak at $\Delta r \approx 3.5r_H$ and the valley at $\Delta r \approx 4.6r_H$ is increasing with time (similarly on the other side of the planet). It is then expected that these changes will become large enough that a threshold is reached and secondary instabilities will be excited.

To demonstrate this, we have made runs out to several hundred orbits (400–800 orbits depending on resolution). Figure 4 shows the evolution of PV in the (r, ϕ) plane for a run with $\mu = 10^{-4}$, $c_s = 0.05$, and $n_r \times n_\phi = 400 \times 1600$. Indeed, a secondary instability is observed to occur in the outer valley of the PV profile at $t \approx 180$ orbits. (The other valley in the $\sim -5r_H$ region also becomes unstable at a later time.) The negative PV regions correspond to the two density bumps, which are roughly axisymmetric early on. When the instability is excited, density bumps break up into ~ 5 anticyclonic vortices (even higher density blobs). Over the next tens of orbits, as the instability evolves and saturates, these density blobs merge, forming density enhancements that are nonaxisymmetric on large scales. This is illustrated in Figure 5 at $t = 500$ orbits. Note that density depression regions also become nonaxisymmetric.

5.2. *Torque Evolution*

As discussed in Koller et al. (2003), one primary goal of studying secondary instability is to understand its impact on the torque evolution of disk gas on the planet. Figure 6 shows the torque
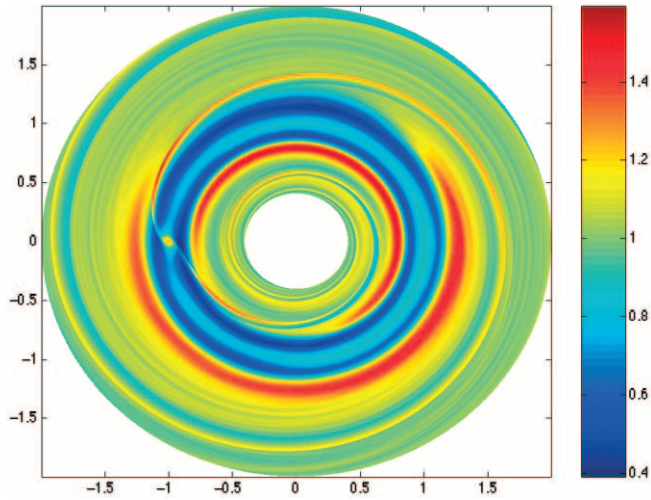
FIG. 5.—Surface density, multiplied by $r^{1.5}$, in the (r, ϕ) plane at $t = 500$ orbits. (Initial surface density is unity at $r = 1$, after multiplying $r^{1.5}$.) After the instability has saturated, the density distribution becomes strongly nonaxisymmetric. When they move around the disk, the torque on the planet oscillates.

history on the planet for a run with the same parameters as in Figure 4. The rapid oscillations in the torque history starting at $t \approx 180$ indicates the initiation of the instability (consistent with Fig. 4). As the higher density blobs pass by the planet, they exert stronger torques. Furthermore, Figure 6 shows that the oscillation amplitude grows with time, which is caused by the gradual density increase in the PV valleys over long timescales. To better understand the origin of fast oscillations, we have calculated the torques separately from three different parts of the disk, which are inner ($\Delta r < 3r_{\rm H}$), middle ($|\Delta r| \leq 3r_{\rm H}$), and outer ($\Delta r > 3r_{\rm H}$), respectively. Figure 7 shows their individual contributions over a time interval $t = 490-512$. We can see that both inner and outer regions have a periodic large amplitude variation. These are caused by the orbital motion of the nonaxisymmetric disk flow at $\Delta r \sim -5r_{\rm H}$ and $\Delta r \sim 7.5r_{\rm H}$, respectively (see Fig. 5). In fact, the torque oscillation periods from these two regions are precisely the expected orbital periods at those radii. Since these two periods are different, their sum gives an erratic appearance (Fig. 6).
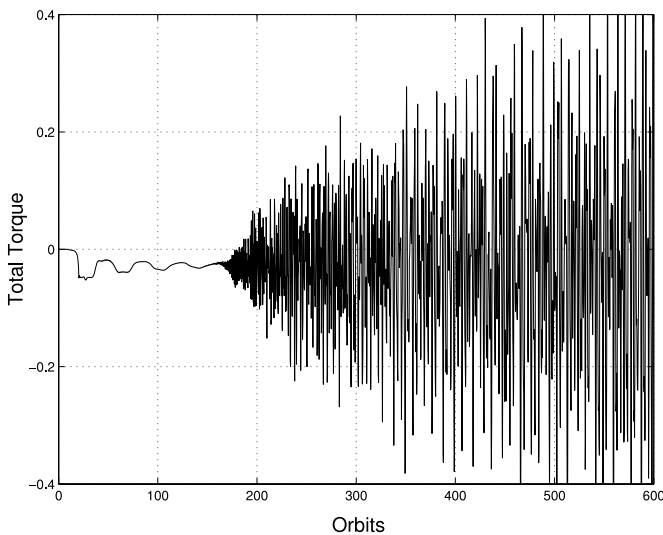

FIG. 6.—Total torque on the planet vs. time from a run having the same parameters as those in Fig. 4. Note that once the flow becomes unstable after $t = 180$, the total torque shows large amplitude oscillations.
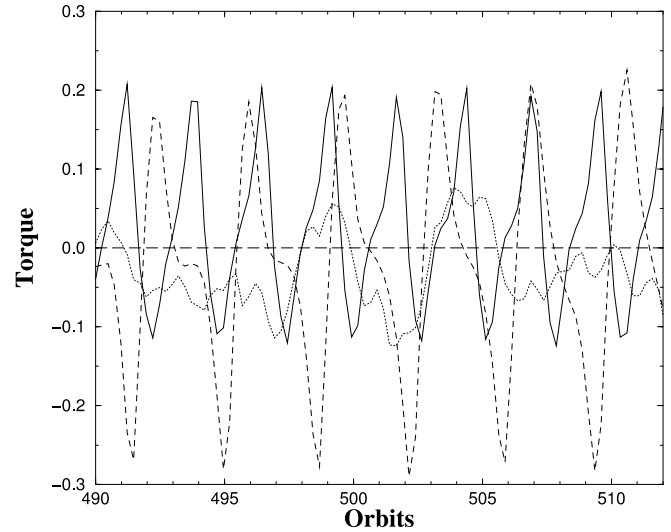

FIG. 7.—Zoomed-in and "decomposed" view of Fig. 6 during orbits $t = 490-512$. The solid, dotted, and dashed curves are torques from three different parts of the disk: $\Delta r < 3r_{\rm H}$, $|\Delta r| \leq 3r_{\rm H}$, and $\Delta r > 3r_{\rm H}$, respectively. The periodic oscillations in torque profiles (solid and dashed curves) are caused by a disk with nonaxisymmetric density profiles rotating around the planet (see Fig. 5). When the higher density region moves close to the planet, it gives a stronger interaction. The oscillation periods in torques are the same as their respective orbital periods.
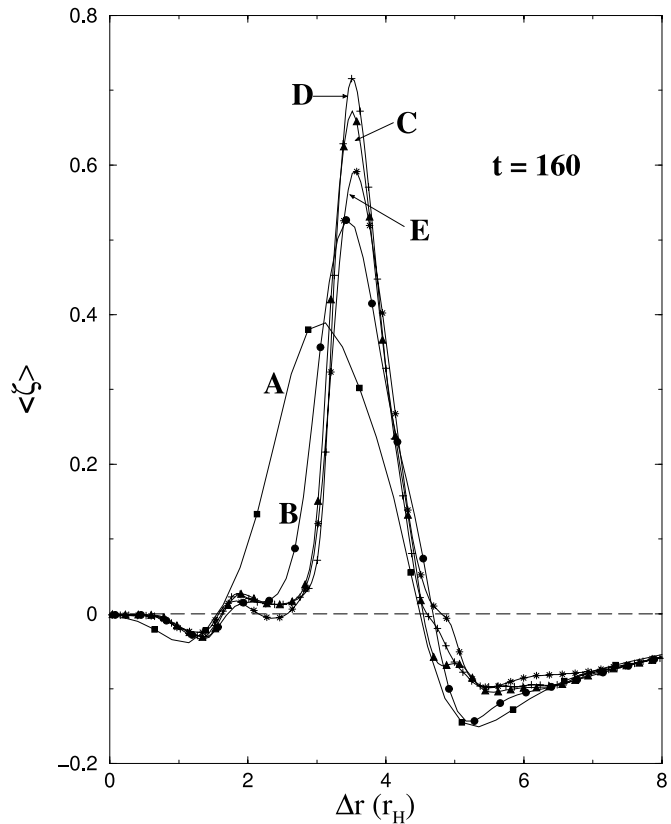

FIG. 8.—Azimuthally averaged $\langle \zeta \rangle$ profile at $t = 160$ orbits with $\mu = 10^{-4}$ and $c_s = 0.05$, but different resolutions: curves A–D use the MHS scheme with $n_r \times n_\phi = 200 \times 800$, 400×1600, 800×3200, and 1200×4800, respectively. Curve E uses the pure Lax-Wendroff scheme with $n_r \times n_\phi = 800 \times 3200$. Curves C and D are quite similar to each other, indicating convergence.
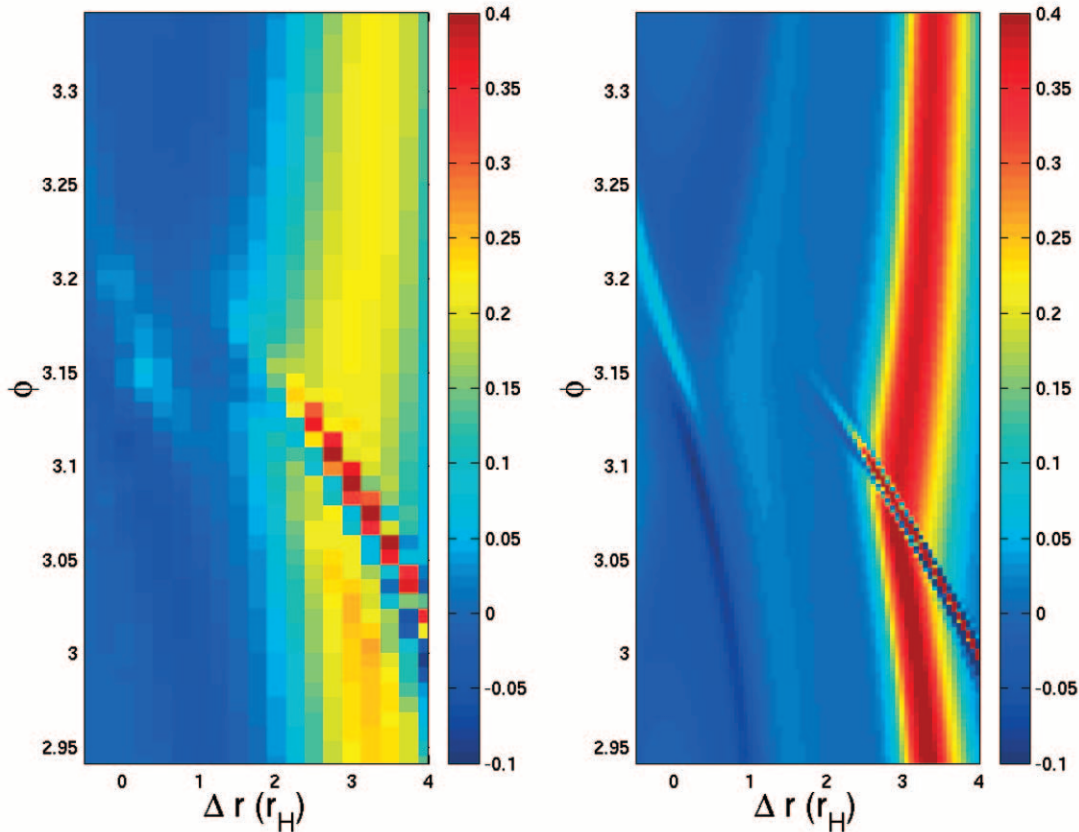
Fig. 9.—PV in the (r, ϕ) plane at $t = 100$ orbits with $n_r \times n_\phi = 200 \times 800$ (*left*) and 800×3200 (*right*). The planet is located at $\Delta r = 0$ and $\phi = \pi$. Only one side is shown. Resolving the shock is important to determining the starting point of the shock and where the PV changes will be deposited.

One might speculate that even with these large amplitudes and rapid oscillations, there seems to be a mean value that is negative and has a small amplitude, consistent with the type I migration expectations. But since our simulations have the planet moving on a fixed circular orbit, it is premature to conclude that these oscillations will not change the type I migration picture. Studies allowing the planet to migrate under the influence of these oscillating torques is under way to address this important issue.

Here we have mostly concentrated on demonstrating the existence of such a secondary instability and its potential impact on the planet's torque. We have not quantitatively analyzed what is the threshold condition in the PV profile that excites this instability. Such a threshold obviously depends on the planet mass, shock structure, sound speed of disk gas, and viscosity in the disk, etc. We have assumed the inviscid limit. Sufficient viscosity could potentially remove the buildup of the PV's peaks and valleys made by shocks, hence never allowing the profile to reach the critical destabilization level.

6. RESOLUTION STUDY

The results we presented here, especially Figures 2 and 4, are different from the findings of Koller et al. (2003; see their Fig. 3, as well as curve A in our Fig. 8). Results there showed additional "dips" interior (i.e., closer to the planet) to the main positive peaks in $\langle \zeta \rangle$. Furthermore, those dips were shown to deepen with time and eventually became unstable.

Figure 8 shows a comparison of runs with four different resolutions but the same set of physical parameters. Even though different curves of $\langle \zeta \rangle$ converge at large Δr ($> 6r_{\mathrm{H}}$) because the

shock is weak and the gradient is small there, the behavior at small Δr (where the shock is strong) shows large differences. Comparing curves A and C, for example, we can see that when the resolution is low and shocks are not well resolved, a larger part of the disk was affected (see the region of $\Delta r \sim 0.5r_{\mathrm{H}}$– $2.5r_{\mathrm{H}}$ in curve A). We were able to reproduce the results of Koller et al. in our low-resolution runs, but our high-resolution studies indicate that the dips observed in Koller et al. are getting narrower and shallower with higher resolutions. This means that the previous results showing the inner dips are numerical artifacts, not true physical effects. Note that the PV within the planet's Roche lobe is not conserved because of both the switch-on of the planet's mass (no matter how slowly) and the numerical error in implementing the planet's potential. This is indicated in Figure 9, where PV in the (r, ϕ) plane at $t = 100$ is shown for two different resolutions. Small PV changes are visible coming out of the planet region. For the low-resolution case, the PV change from the planet is "spread" over a wide region. It is then amplified by poorly resolved shocks. Such amplification eventually leads, unfortunately, to an instability, in much the same spirit we have discussed here. For the high-resolution run, the shock and the PV change from the planet is well separated. The erroneous amplification does not occur.

We see that very high resolutions (800×3200 to 1200×4800) are needed to obtain convergence in the $\langle \zeta \rangle$ profile (curves C and D). We emphasize that even though there are still some minor differences for the high-resolution runs we presented here, the overall feature of having a positive peak and a negative valley is quite consistent among all resolutions. Furthermore, the instability now comes out of the valley region, which typically has a much better

convergence than other parts of the ζ profile. In addition, we have also made a run using pure a Lax-Wendroff scheme with $n_r \times n_\phi = 800 \times 3200$ (curve E). Compared with curve C, it gives very similar results. It also shows the instability at later times (not shown here), although the MHS scheme gives sharper and smoother shocks than hybrid schemes.

7. CONCLUSIONS

We have carried out high-resolution, two-dimensional hydrodynamic disk simulations with one embedded protoplanet. We find that the total torque on the planet, caused by tidal interactions between the disk and the planet, can be divided into two stages. First, it is negative and slowly varying, consistent with the type I migration expectation. Second, it shows large amplitude and very fast oscillations as a result of the excitation of an instability that first breaks up the axisymmetric density enhancement into higher density blobs, e.g., vortices. These vortices then merge, forming large-scale nonaxisymmetric density enhance-ments. This nonaxisymmetry causes the torque to continuously oscillate.

In Koller et al. (2003), we were misled by a spurious feature in the PV profile, owing to an inadequate numerical resolution, which eventually became unstable. Despite the inaccurate location where a secondary instability is initiated, the physical explanation proposed by Koller et al. for exciting such an instability is well founded. We now have a self-consistent picture from performing very high resolution simulations for understanding the shock structure and the PV profile. Further studies allowing the planet to migrate under the influence of these torques will be necessary as well as very interesting.

REFERENCES

Balmforth, N. J., & Korycansky, D. G. 2001, MNRAS, 326, 833
D'Angelo, G., Kley, W., & Henning, T. 2003, ApJ, 586, 540
Drazin, P. G., & Reid, W. H. 1981, Hydrodynamics Stability (Cambridge: Cambridge Univ. Press)
Goldreich, P., & Tremaine, S. 1979, ApJ, 233, 857
———. 1980, ApJ, 241, 425
Kevlahan, N. K.-R. 1997, J. Fluid Mech., 341, 371
Kley, W. 1998, A&A, 338, L37
———. 1999, MNRAS, 303, 696
Koller, J., Li, H., & Lin, D. N. C. 2003, ApJ, 596, L91
Korycansky, D., & Papaloizou, J. C. B. 1996, ApJS, 105, 181
Li, H., Colgate, S. A., Wendroff, B., & Liska, R. 2001, ApJ, 551, 874
Lin, D. N. C., & Papaloizou, J. 1986a, ApJ, 307, 395
———. 1986b, ApJ, 309, 846
Lubow, S. H., Seibert, M., & Artymowicz, P. 1999, ApJ, 526, 1001
Masset, F. S. 2000, A&AS, 141, 165
———. 2002, A&A, 387, 605
Nelson, R. P., Papaloizou, J. C. B., Masset, F., & Kley, W. 2000, MNRAS, 318, 18
Tanigawa, T., & Watanabe, S. 2002, ApJ, 580, 506
Toro, E. F. 1999, Riemann Solvers and Numerical Methods for Fluids Dynamics (2nd ed.; Berlin: Springer)
Ward, W. R. 1997, Icarus, 126, 261